Full Length Article

Photocatalytic dye removal with ZnO/Laser-Induced graphene nanocomposite

Regina Del Sole [a], Alexander Dallinger [b], Birgit Kunert [b], Sreenadh Thaikkattu Sankaran [c,d], Francesco Greco [b,c,d,e], Paola Parlanti [f], Mauro Gemmi [f], Antonella Milella [a,g], Francesco Fracassi [a,g], Anna Maria Coclite [b,h,*]

[a] *Dipartimento di Chimica, Università degli Studi di Bari Aldo Moro, Via Orabona 4, 70126, Bari, Italy*
[b] *Institute of Solid State Physics, NAWI Graz, Graz University of Technology, Petersgasse 16, 8010 Graz, Austria*
[c] *The Biorobotics Institute, Scuola Superiore Sant'Anna, Viale R. Piaggio 34, 56025 Pontedera, Italy*
[d] *Department of Excellence in Robotics & AI, Scuola Superiore Sant'Anna, Piazza Martiri della Libertà 33, 56127 Pisa, Italy*
[e] *Interdisciplinary Center on Sustainability and Climate, Scuola Superiore Sant'Anna, Piazza Martiri della Libertà 33, 56127 Pisa, Italy*
[f] *Center for Materials Interfaces, Electron Crystallography, Istituto Italiano di Tecnologia, Pontedera, Italy*
[g] *CNR-NANOTEC, c/o Dipartimento di Chimica, Università degli Studi di Bari Aldo Moro, Via Orabona 4, 7012, Bari, Italy*
[h] *Dipartimento di Fisica, Università degli Studi di Bari Aldo Moro, Via Orabona 4, 70126, Bari, Italy*

ARTICLE INFO

ABSTRACT

ZnO has been deposited on Laser Induced Graphene (LIG) by Atomic Layer Deposition (ALD) running up to 100, 200 and 400 number of cycles. Two different LIG substrates have been used, which differed by their porosity degree. The ALD technique allows to grow ZnO stoichiometrically on the chosen substrates down to the bottom of the pores of the material, guaranteeing an increasing coverage with increasing number of deposition cycles. The crystallinity of the deposited ZnO is also proven via XRD analysis. The photocatalytic activity of the ZnO@LIG nanocomposites has been evaluated through monitoring the discoloration of a 10^{-5} M methylene blue (MB) solution upon UV irradiation ($\lambda = 365$ nm) over a time span of 120 min. Results indicate that the photocatalytic performance of the nanocomposites increases with the ZnO deposition time. For nanocomposites showing the higher ZnO coverage degree, after 120 min of irradiation a net MB photodegradation percentage of 71 ± 4 % and 69 ± 4 % is reached respectively for the less porous and more porous substrate. Conversely, the MB adsorption percentage of the samples decreases upon ZnO deposition, due to the reduced accessible porosity and the hydrophobicity of the nanocomposites. The method used to produce such solid supported nanocomposites is straightforward and represents a valuable option to obtain efficient environmental-friendly photoactive materials.

1. Introduction

The study of nanocomposite materials has received increasing attention in recent decades because new properties arise from the combination of their components, thus resulting superior to those of the single constituents. Among inorganic nanomaterials, semiconductors have been extensively investigated for their optoelectronic properties. In particular, zinc oxide (ZnO), an n-type semiconductor, shows good chemical and thermal stability and it is nontoxic, low-cost, abundant in nature and has remarkable electrical and optical properties. Indeed, ZnO nanostructures possess exemplary photosensitivity due to unique

properties, first and foremost its wide band gap (3.37 eV) that leads to a strong absorption in the UV region. For these reasons, ZnO-based nanomaterials appear to be suitable for photocatalysis applications that include the degradation of organic pollutants in different matrices and resulting in effective water treatment. ZnO is considered as the second more widely used photocatalyst after TiO_2, as it also exhibits antifouling and antibacterial properties along with photocatalytic ones [1,2]. A common drawback of ZnO, shared with other n-type semiconductors, is its fast electron-hole recombination rate that limits the photocatalytic performances [3]. In order to encompass such limitation, a viable solution is to use carbon-based nanomaterials as co-catalysts in

---

nanocomposites with ZnO, [4,5]; thanks to their work function (e.g., 4.3 eV for graphene [6]), they act as an electron trap, increasing the lifespan of electron–hole pairs. Moreover, the photoelectrons can be more effectively delocalized through their extensively conjugated network of carbon atoms, thus contributing further to the reduction of the charge recombination phenomenon [7].

Going into further detail, a particularly interesting and relatively novel carbon nanomaterial that could serve this purpose is Laser Induced Graphene (LIG). LIG was first investigated in greater detail in 2014 by Lin et al. [8] showing the preparation of three-dimensional porous graphene with large specific surface area ($\approx$340 m^{2}g^{-1}), high thermal stability (>900 °C) and excellent conductivity (5–25 Scm^{-1}) by direct laser-induced pyrolysis of commercial polyimide (PI), using a CO$_2$ infrared laser scribing system. This process is carried out under ambient conditions, without the need for material pre-treatment, and at a low cost. Laser scribing of polyimide allows to circumvent the high temperatures and vacuum requirements of conventional graphene synthesis. In contrast to the conventional hexagonal honeycomb carbon network observed in two-dimensional (2D) graphene, LIG's atomic arrangement features pronounced distortion of the six-membered rings. This irregular structure, coupled with a multitude of disorders and grain boundaries, contributes to LIG's properties, which distinguishes it from 2D graphene [9]. In addition, LIG synthesis and patterning is provided within a single step and allows to obtain complex patterned structures both on flexible and rigid substrate, opening to new scenarios for wide-ranging applications, such as flexible and wearable electronics, robotics, smart clothing, and electronic skins [10]. The morphology and properties of the resulting LIG can be modulated by tuning properly the laser scribing parameters, such as the speed, power, frequency/density of scribed points, and defocus. The morphology ranges from porous structures with different pore sizes to micrometer sized, needle-like structures emerging from the surface [11–14]. Most recent frontiers of LIG research, include the use of other polymers and even bioderived and renewable precursors such as various lignocellulosic materials (e.g. wood, clothes, and food waste), in order to make this material more environmentally friendly and low-cost as possible, for widespread application [15].

For conveniently addressing environmental applications, such as the photodegradation of organic pollutants in wastewaters, the technological issues of the separation and subsequent reuse of the nanomaterials need to be solved, thus highlighting the urge to immobilize them on a solid support. Moreover, porous photocatalysts should be preferred, when possible, as they offer several advantages. First and foremost, they show abundant active sites and a high surface area that allow the incorporation of (nano)particles or photosensitizers into the pores, leading to a higher loading and thus better photocatalysis performances [16,17]. While for thin films the large photo-generation of electron-hole pairs that migrate to the surface plays an essential role in defining the photocatalytic activity of the material, in the case of 3D porous photocatalysts other key factors become relevant. For instance, an increased specific surface area promotes adsorption and photocatalytic reactions. By exposing more reactive sites, and thereby accelerating the surface photocatalytic reactions, it plays an essential role in eliminating the environmental pollutants in the liquid phase owing to the cooperation of adsorptive enrichment and photocatalysis. As the thin film is deposited on an intricate 3D structure conformally, the morphological complexity is retained upon deposition and continues to be a crucial aspect to be considered in the description of the photocatalytic activity of the photocatalyst [18]. Also, porous photocatalysts show an efficient mass adsorption and diffusion, and an enhancement of the light harvesting.

In metal oxides/LIG nanocomposites, LIG can play not only the role of co-catalyst. Indeed, the use of LIG as a substrate implies a rise in the surface area and increased amount of the photocatalyst. Also, the solid nature of the substrate allows for the convenient use of the nanocomposite as a free-standing photocatalyst for the photodegradation of organic pollutants in water as it facilitates its removal from the reaction media and allows its easy re-use. A significant photocatalytic performance was demonstrated for TiO$_2$/LIG nanocomposites [19]. Moreover, ZnO/LIG nanocomposite films, obtained via doctor blade [20], or by electrodeposition [21] have already been extensively characterized, demonstrating that a successful application of these composites is dependent on controlling the quality and characteristics of the LIG/ZnO interface (e.g. thickness of ZnO) and whether the desired electrochemical and/or optical properties are achieved. For this reason, the synthesis and characterization of these nanocomposites must be deeply understood to achieve reproducible properties.

In this perspective, we decided to investigate Atomic Layer Deposition (ALD) of ZnO on LIG. This technique could represent a favorable alternative to the methods of deposition of ZnO on LIG presented so far. ALD allows to keep complete control on the thickness of the deposited layer and it can create high-quality thin film with good conformality: it is exceptionally effective at coating surfaces that exhibit ultra-high aspect ratio topographies, as well as surfaces requiring multilayer films with good quality interfaces [22]. In this study for the first time thermal ALD of ZnO is performed on LIG substrates for the preparation of nanocomposite photocatalysts. Two morphologically distinct LIG types, both synthesized via laser-induced pyrolysis but with different laser scribing parameters, are employed as substrates for ZnO. The characterization and photocatalytic performance of ZnO/LIG nanocomposites toward the degradation of organic pollutants under UV irradiation are then compared.

2. Experimental section

2.1. LIG preparation

Two morphologically distinct LIG substrates were used and labeled as LIG-P and LIG-V. While LIG-P consists of a thinner layer with smaller pores, LIG-V is thicker and exhibits larger pores in comparison (Supporting Information, SI, Fig. 1S). The preparation of LIG-P is described from Dallinger et al. [12]. A laser cutter/engraver (Universal Laser Systems VLS 2.30, Power 30 W) operating with a CO$_2$ laser source at 10.6 μm wavelength and equipped with an HPDFO (High-Power Density-Focusing Optics) beam collimator (nominal beam size in focus: 25.4 μm) was used to create conductive patterns of LIG onto PI tape (Kapton HN, thickness = 50 μm, with silicone glue, supplied by M&S Lehner GmbH). PI tape was attached to glass microscope slides (25 × 75 × 1 mm, ISO 8037/1, Epredia) for easier manipulation of samples. The following settings of laser rastering parameters were employed for producing LIG-P: Power P = 10 %, Scribing Speed S = 10 %, raster resolution of 500 PPI, image density (ID) of 5 (arbitrary scale, defining a spacing between consecutive rastered lines of ~50 μm), and a positive defocusing of Z = 0.7 mm. Parameters for LIG-V were the following: Power P = 28 %, Scribing Speed S = 50 %, raster resolution of 500 PPI, image density (ID) of 5, and a positive defocusing of Z = 0.1. At the end of the process, all the samples produced and the ALD-treated consisted in 2.0x2.0 cm LIG area scribed onto a 2.5x2.5 cm PI piece.

2.2. ALD deposition of ZnO: ZnO@LIG nanocomposite

A custom-built ALD reactor [23] was used to deposit the ZnO thin films on single side polished c-Si (100) substrates (Siegert Wafer) for the development of the ideal deposition recipe, and on LIG substrates. Diethyl zinc (DEZ, Sigma-Aldrich) was used as the metalorganic precursor and H$_2$O was used as co-precursor. A constant flow rate of Ar (16 sccm) was adopted during the whole process as purging and carrier gas. An automation platform (MKS PAC 1000) and a mass flow controller (MKS MF1-C) were used to control the Ar flow rates. ALD-valves (Swagelok ALD3) were used to pulse DEZ and H$_2$O into the reactor. No further heating or bubbling system were adopted for DEZ and H$_2$O. The whole process was carried out at 110 °C (T$_{reactor}$) and the DEZ and H$_2$O lines were heated at 60 °C. The thickness of the ZnO layer deposited on control Si wafer was measured via spectroscopic ellipsometry (J.A.

Woollam M−2000 V). The measurements were carried out at three different angles (65°, 70°, and 75°) in the wavelength range from 370–1000 nm. The analysis of the spectra was performed with the software CompleteEASE® by applying a three-layer model consisting of a silicon substrate, a native silicon oxide layer with a fixed thickness of 1.5 nm and a Cauchy model for ZnO in which the wavelength-dependent refractive index n is calculated as follows:

$$n(\lambda) = A + \frac{B}{\lambda^2} + \frac{C}{\lambda^4}$$

with λ being the wavelength and A, B, and C fit parameters. These parameters were fitted in the spectral range 450–1000 nm in order to use only the ZnO transparent region. The Growth Per Cycle (GPC) was determined by averaging the thickness of at least 3 samples placed on the sample holder and dividing it by the number of cycles. The saturation curves built in this preliminary phase are reported in Supplementary Information (Fig. 2S). The optimized thermal ALD recipe consisted of the sequence < DEZ pulse/ Ar purge/ H₂O pulse/Ar purge > with pulse times < 0.15/15/0.15/50 > in seconds.

After the optimization of the deposition parameters, LIG-P and LIG-V were used as substrates for producing ZnO@LIG nanocomposites. The depositions were run up to 100, 200 and 400 ALD cycles.

2.3. Characterization of ZnO@LIG nanocomposites

Scanning Electron Microscopy (SEM) micrographs were obtained with a Phenom XL SEM by ThermoFisher Scientific (secondary electron detector) operating at 10 kV and equipped with Energy-dispersive X-ray spectrometer. A Focused Ion Beam Scanning Electron Microscope (FIB-SEM) Helios Nano Lab 600i (Thermo Fisher Scientific, Waltham, MA, USA), equipped with a Bruker XFlash Detector 5010 for Energy-dispersive X-ray spectroscopy (EDX), was used for characterizing the LIG samples in cross section. Cross-sections of the material were obtained using the gallium beam impinging perpendicularly on to the sample's surface and operating at 30 kV and 21–65 nA. SEM images were acquired with an Everhart–Thornley detector (ETD) working at 5 kV and 45 pA landing current using secondary electrons (SE) detection. For cross sections imaging, samples were kept at a working distance of 4–4.2 mm and either 52° or 30° tilt (respectively, LIG-P ZnO and LIG-V ZnO) respect to electron beam. Surface chemical composition was investigated by XPS analyses with a PHI 5000 Versa Probe II spectrometer (Physical Electronics) equipped with a monochromatic Al Kα X-ray source (1486.6 eV), operated at 15 kV and 24.8 W, with a spot size of 100 μm. Survey (0–1200 eV) and high-resolution spectra (C1s, O1s, N1s and Zn2p) were recorded in FAT (Fixed Analyser Transmission) mode at a pass energy of 117.40 eV and 29.35 eV, respectively. Surface charging was compensated using a dual beam charge neutralization system, with a flux of low energy electrons (~1 eV) combined with very low energy positive Ar⁺ ions (10 eV). All binding energies were referenced to the C1s core level photoemission line at 284.6 eV. All spectra were collected at an angle of 45° with respect to the sample surface. Curve fitting of the high-resolution spectra was carried out with Multi-Pak data processing software (Physical Electronics) using a Shirley background and Gaussian/Lorentzian peak shape. Sputtering depth profiling was carried out on ZnO films deposited onto Si to investigate the in-depth distribution of carbon and to determine the exact film stoichiometry across the whole film thickness, and it was accomplished with 1 kV, 1 μA Ar⁺ ion gun, with a raster size of 2x2 mm².

XRD measurements were performed in in a Θ/Θ-configuration with a Panalytical Empyrean diffractometer (PANalytical, the Netherlands, Cu tube, λ = 1.5418 Å). The same samples i.e., PI tape with laser scribed LIG on top of a glass substrate, were used. The peaks for the comparison with the expected materials were generated using the Inorganic Crystal Structure Database (ICSD), PowderCell and DIFFRAC.EVA. The crystallite size was calculated using the Scherrer equation [26]:

$$\tau = \frac{K \times \lambda}{\beta cos\theta}$$

with τ being the crystallite size, K being a shape factor (K = 1), λ being the X-ray wavelength (λ = 1.5418 Å), β being the full width at half maximum of the corresponding peak and θ being the Bragg angle (2Θ/2).

Water contact angle (WCA) measurements were carried out using a Rame'-hart 100 manual goniometer. The WCA was calculated as the average between 3 drops (with 2 μL volume) on each sample surface.

2.4. Photocatalytic activity evaluation of ZnO@LIG nanocomposites

The photocatalytic activity of the nanocomposite coatings was evaluated through monitoring the discoloration of a model pollutant (methylene blue, MB, Sigma Aldrich, Darmstadt, Germany) solution by means of a UV–Vis spectrophotometer (Shimadzu UV-1800 Spectrometer). Spectra were collected in slow mode in the 450–800 nm range in polystyrene semi-micro cuvettes. ZnO@LIG samples prepared on microscope slide glasses were placed at the bottom of a 50 mL beaker. Next, 5 mL of MB 10⁻⁵ M solution were poured in the beaker with a diameter at the bottom of 4 cm. The solution was placed under magnetic stirring by means of an 8 mm PTFE magnetic bar that was placed on the bottom the beaker. As the dimensions of the sample is 2.5 cm x 2.5 cm, the magnetic bar was able to rotate freely in a decentred position without damaging the samples at the bottom. The solution was then left in the dark for 15 min as a conditioning step. Absorbance at 665 nm, corresponding to the characteristic peak of MB, was measured for the prepared solution after the conditioning step to isolate the contribution of the adsorption of MB on the photocatalyst surface due to the discoloration process. Then, the system was irradiated from above by means of a 6 W UV lamp (VILBER VL-6.L, λ = 365 nm, irradiance 0.700 mW/cm²) set at a distance of 13 cm from the substrate. Absorbance at 665 nm was measured at defined intervals of time up to 120 min; the evaporation was negligible in this time span. The discoloration percentage [24], was calculated using the following equation:

$$\%discoloration = \left[100 - \left(\frac{Abs_t * 100}{Abs_{t_0}} \right) \right]$$

where Abs_{t0} is the absorbance measured after the conditioning step and Abs_t is the absorbance value at a given time. The same procedure was then repeated in dark conditions using a replicate for each sample, obtaining adsorption curves. Finally, the contribution of the photodegradation of the dye to the total discoloration was evaluated on the basis of the difference between the discoloration curves measured under UV irradiation and in dark conditions corresponding to the same sample (collected on two replicates) (as reported in supporting information, Figure 10S).

3. Results and discussion

The thickness of the deposited ZnO was measured on control Si wafers placed inside the reactor during the deposition on LIG. The results are reported in Table 1S (Supporting Information, SI). These could be considered as nominal thicknesses for the ZnO deposited on LIG since a direct measurement of the ZnO thickness grown on LIG by ALD was non trivial due to the LIG's porous nature. Nevertheless, especially on the more porous LIG, the deviation from this nominal thickness could be relevant.

3.1. ZnO@LIG nanocomposites characterization

Scanning electron microscope (SEM) images of bare and ZnO-coated LIG-P with different cycles are shown in Fig. 1a. The porous structure of bare LIG-P shown in the first column becomes more and more covered
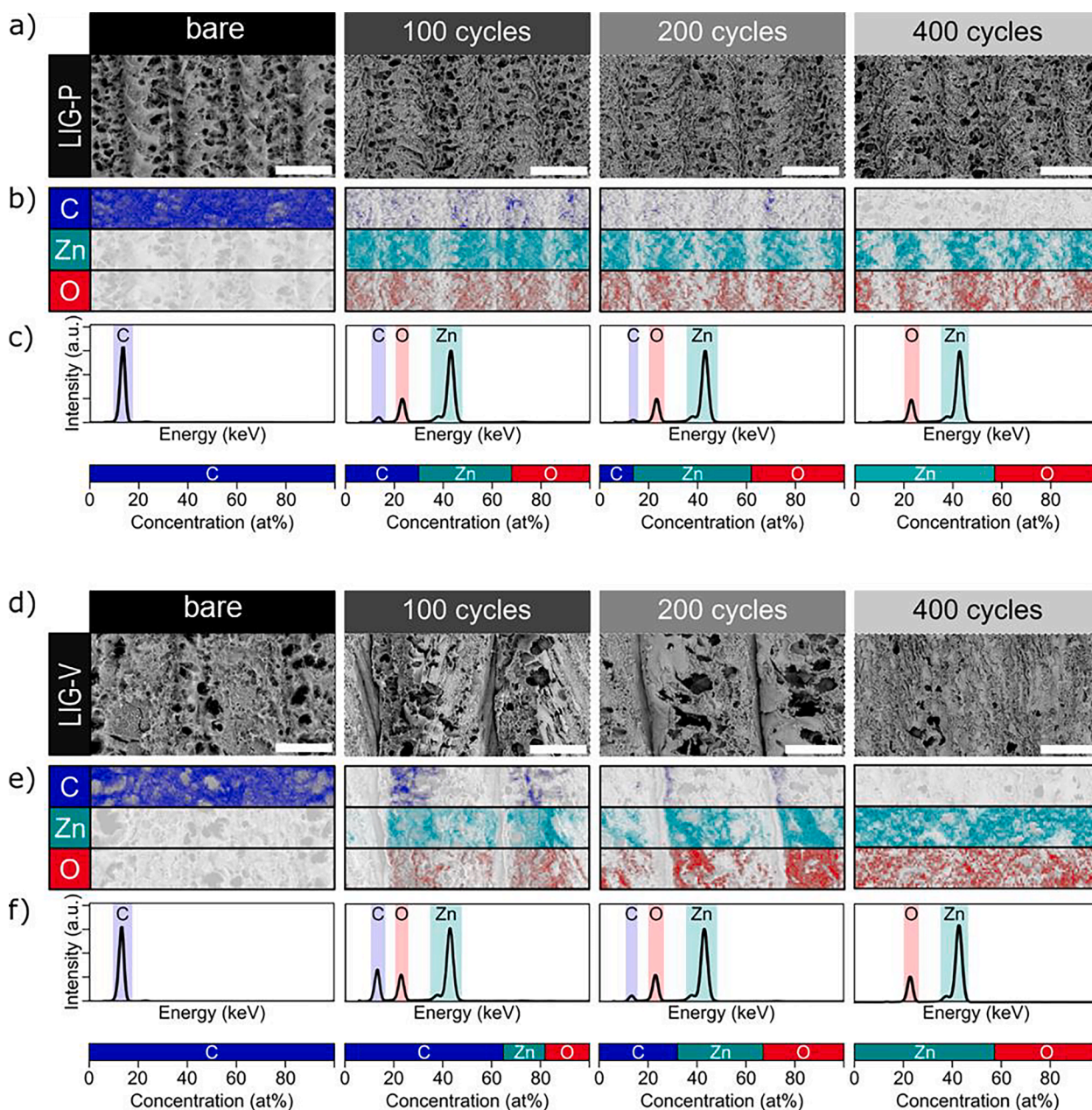
Fig. 1. A) SEM images of bare LIG-P and at different ALD cycles of ZnO coating (scale bar = 50 μm), **b)** corresponding EDX elemental maps showing the distribution of C, Zn and O, **c)** corresponding EDX spectra and concentration in at%, **d)** SEM images of bare LIG-V and at different ALD cycles of ZnO coating (scale bar = 50 μm), **e)** corresponding EDX elemental maps showing the distribution of C, Zn and O, **f)** corresponding EDX spectra and concentration in at%. The images of the elemental map are divided in three strips each corresponding only to one element.

with ZnO, at increasing number of ALD cycles. As the number of ALD cycles increases and more ZnO is deposited, the accessible porosity decreases significantly, both in terms of the number of pores and the diameter dimension.

Energy dispersive X-ray (EDX) analysis provides a clearer visualization of the progressive growth of ZnO with increasing number of ALD cycles. In Fig. 1b, EDX mapping is reported for LIG-P. The images show that the ZnO coverage of the LIG surface increases with the number of ALD cycles as expected. At 400 cycles the ZnO layer is thicker, and carbon signal is not detected anymore.

A similar trend is observed for LIG-V (Fig. 1d) where the porosity decreases with increasing ALD cycles and ZnO thickness. However, LIG-V shows pores with larger diameter compared to LIG-P. Interestingly, at 400 cycles hardly any pores are visible at the surface for LIG-V. The EDX mapping for LIG-V shows a higher amount of C compared to LIG-P for

the same number of cycles. This is probably due to the higher surface area of LIG-V, leading to the deposition of a thinner coating over the whole surface during the ALD process. Nonetheless, similarly to the LIG-P case, the carbon signal is not detected anymore at 400 ALD cycles.

Higher magnification SEM images of LIG-P and LIG-V (Figures 4S, SI) show that both exhibit a finer nanostructure on the ZnO@LIG surface after ZnO deposition compared to the pristine material. This fine-grain structure after the ZnO deposition is relatable to the formation of ZnO nanoparticles.

The above reported EDX characterization can only provide information about the surface of the ZnO@LIG samples, but nothing is known about the internal porous structure, whether ZnO coating is grown inside it and how deep. To fully characterize the structure morphology of the ZnO@LIG samples in depth, focused ion beam (FIB) milling and SEM of cross-sections were used, (Fig. 2a and b). In combination with EDX
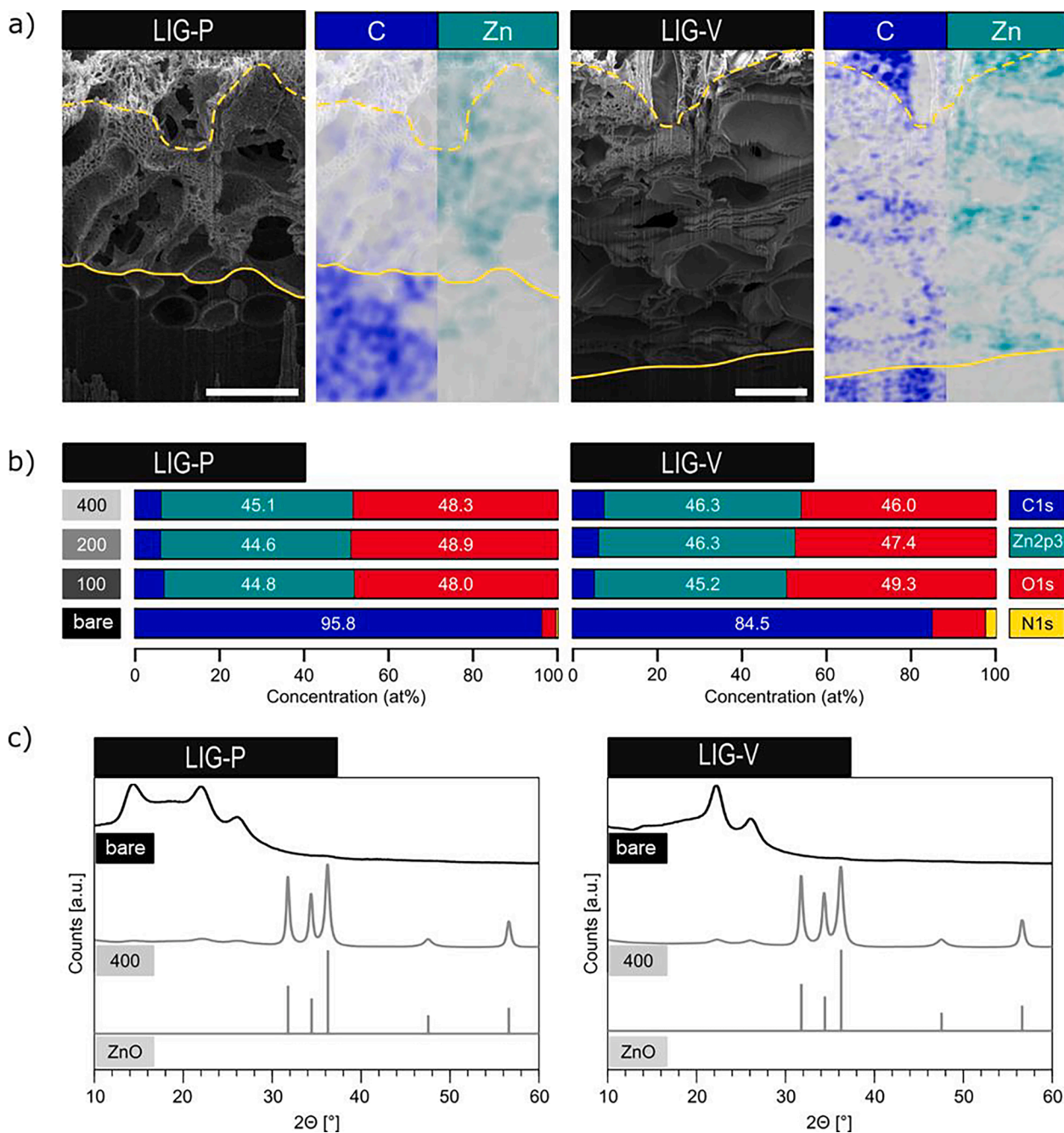
Fig. 2. A) SEM micrographs of FIB cross-sections of LIG-P and LIG-V coated with 100 ALD cycles of ZnO and distribution of C and Zn via EDX mapping. The sample surface is shown by yellow dashed line, and PI substrate/LIG interface is shown by the solid yellow line (scale bar = 10 µm) b) XPS results showing the at% of Zn, O, N and C for bare LIG and ZnO@LIG nanocomposites with different ALD cycles (100, 200 and 400), c) XRD results for bare and 400 ALD cycles of ZnO coating for LIG-P, LIG-V and theoretical peak positions for ZnO (PDF#89–0510) [27].

elemental maps, they enable the examination of the composition of the bulk material and the depth of ZnO deposition within the LIG after 100 ALD cycles. In both cases, for LIG-P and LIG-V, the whole thickness of LIG was FIB-cross sectioned, as evidenced by the darker and marked areas on the bottom of the images showing the PI substrate. A total LIG thickness of $d_{LIG-P} = 21.1 \pm 3.0$ µm and $d_{LIG-V} = 77 \pm 14$ µm could be estimated from these cross-sectional images for the two substrate types.

The EDX elemental maps for C and Zn overlaid on the SEM image clearly indicate that Zn is present throughout the entire depth of the LIG for both LIG-P and LIG-V at 100 ALD cycles. Sometimes, the coating even filled the pores in the PI substrate, generated by the heat during laser-induced pyrolysis. In the case of LIG-P, a signal of Zn is detected

below the substrate/LIG interface (yellow solid line).

High magnification SEM micrographs of bare LIG-P and LIG-V and at 100 ALD cycles (Figure 5S, SI) show that the overall pore structure remains the same, but the surface of the pores is covered with a nanostructured layer.

These findings show that ZnO is deposited all around the surface of the pores, to the very bottom of the LIG samples. This means that the ALD process is efficient to deposit conformal coatings even on very porous and relatively thick 3D substrates such as LIG throughout the whole bulk material.

X-ray photoelectron spectroscopy (XPS) was used to provide more detailed information about the chemical composition of the sample

surface. The measurements show a nearly stoichiometric growth of ZnO already at 100 cycles (O/Zn ratio of 1.07 for LIG-P and 1.09 for LIG-V), for both LIG substrates. The ratio is not changing with increasing cycles for both types, as reported in Fig. 2b.

The stochiometric growth of ZnO was further checked by analyzing control Si wafer placed next to LIG samples inside the reactor chamber giving an O/Zn ratio of 1.00 ± 0.02 for all samples. More details are reported in Supporting Information (Figure 3S).

X-ray diffraction experiments gave further insight into the crystallographic properties of the deposited ZnO (Fig. 2c). For both species, LIG-P and LIG-V the bare samples only showed peaks characteristic for the PI polymer substrate (see Figure 6S, SI). The samples with 400 ALD cycles of ZnO coating showed distinct peaks belonging to ZnO [26] and only very weak peaks corresponding to the PI substrate.

On the other hand, it is noteworthy that there is a conspicuous absence of any significant peak for LIG. This can be attributed to its low crystallinity, which is also evident in the Raman spectroscopy data from a previous work conducted on the substrate ($I_D/I_G > 1$) [12] and from SEM images.

By using the Scherrer equation the crystallite size of the ZnO can be estimated to 16.9 ± 5.5 nm for ZnO@LIG-P and 15.6 ± 5.3 nm for ZnO@LIG-V [26]. Values for each peak can be found in the Supporting Information in Tables 2S and 3S.

3.2. ZnO@LIG nanocomposites photocatalytic activity

The adsorption capacity of the samples was evaluated by determining via UV–Vis spectroscopy the dye discoloration percentage in absence of UV irradiation over 120 min. Fig. 3a displays the results at 120 min for ZnO@LIG-P and ZnO@LIG-V nanocomposites as well as the bare LIG-P and LIG-V. Bare substrates showed the highest MB adsorption, with LIG-V exhibiting even higher adsorption due to its higher porosity. Upon ZnO deposition the adsorption capacity drastically decreases. In particular, the adsorption decreases with the number of ZnO deposition cycles. This is compatible with the total coverage of the LIG substrate by ZnO, whose adsorption capacity is not significant [28]: the coating lowers the accessible porosity of the material, as observed by SEM images (Fig. 1a and d). In addition, the water contact angle (WCA) ϕ was measured for the bare samples, giving values of $\phi_{LIG-P} = 43 \pm 11°$ and $\phi_{LIG\_V} = 57 \pm 8°$. After 400 cycles of ZnO deposition, the WCA increased significantly to $\phi_{LIG-P} = 146 \pm 11°$ in the case of LIG-P. For LIG-V no value could be measured as the droplet could not be deposited
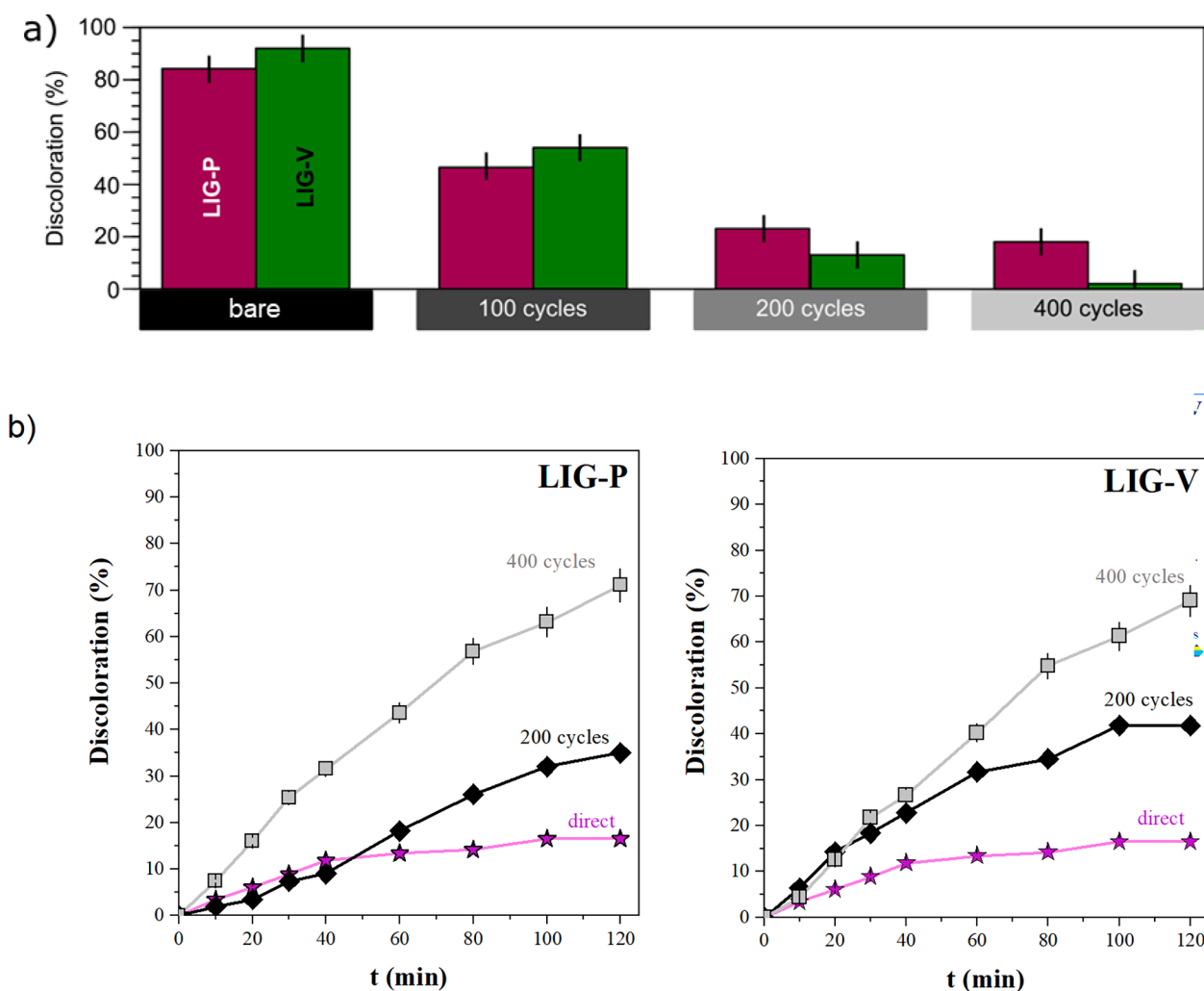

Fig. 3. **A)** Discoloration of the MB solution due to adsorption at 120 min (no UV light resulting in no photolysis). **b)** Discoloration of MB solution due to photolysis with ZnO@LIG-P coated with 200 and 400 ALD cycles and direct photolysis without any catalyst. **c)** Discoloration of MB solution due to photolysis with ZnO@LIG-V coated with 200 and 400 ALD cycles and direct photolysis without any catalyst. It is worth noting that the Fig. 3b does not include the photocatalytic activity of the nanocomposites obtained at 100 ALD cycles. This is related to the strong adsorption capacity of these samples. As can be observed in further detail in Figure 10S, the adsorption curves for these samples do not even reach a plateau within the time range explored, therefore making meaningless the calculation of the photocatalytic activity performed via the method applied for the nanocomposites obtained at 200 and 400 ALD cycles, which instead show a steady adsorption.

on the surface and stayed on the needle of the goniometer, evidencing an extreme superhydrophobic behavior. The WCA of the ZnO deposited on a Si control sample showed a value of $\phi = 94 \pm 6°$. This increase in WCA can be ascribed to the hydrophobicity of the deposited ZnO coating and the formation of nanostructures with consequent roughening of the surface [25]. The high roughness of the resulting coating is further enhanced by the effect of the intrinsic roughness of the starting supporting material as in the case of LIG [12]. It is worth highlighting that in general an increase in the water contact angle limits the photocatalytic performance of the material [29], as it is also correlated to the efficient cooperative adsorption of the dye onto the catalyst surface.

On the other hand, it is important to note that upon exposure to UV light, both bare LIG-P and LIG-V exhibit no photocatalytic activity as expected (Figure 7S). In contrast, a ZnO control sample deposited for 400 ALD cycles on PI substrate showed a slight photocatalytic activity (Figure 8S) as evidenced by the slightly greater discoloration compared to just UV exposure of the solution without any ZnO present.

To separate the adsorption contribution from the photocatalytic activity of the ZnO@LIG nanocomposites, the adsorption curves were subtracted from the discoloration curves recorded in the presence of UV irradiation, as described in the experimental section.

Fig. 3b and c show the resulting photodegradation curves for MB in ZnO@LIG nanocomposites. The photocatalytic activity of LIG-P increases with the number of ALD cycles, with the highest degradation (71 $\pm$ 4 %) observed for the sample obtained at 400 ALD cycles at 120 min. The photodegradation performances of the samples obtained at 200 cycles are significantly lower (35 $\pm$ 2 %). This is consistent with the results obtained by EDX mapping, which detected higher C and lower Zn and O concentrations if compared to the 400 cycles nanocomposite (Fig. 1c), thus pointing out the lower degree of coverage.

In a similar fashion, the discoloration of MB for ZnO@LIG-V increases with the number of ALD cycles, reaching a value of 69 $\pm$ 4 %. This value is not significantly different from the one obtained for ZnO@LIG-P nanocomposite at 400 ALD cycles (71 $\pm$ 4 %), but in both cases an increase of the photocatalytic activity is observed with increasing ZnO ALD cycles. These results of ZnO@LIG-V are compatible with the EDX mapping, which shows a surface completely covered in ZnO for both samples and XPS results for Zn and O at%, which are the same for the ZnO@LIG-P nanocomposite deposited under the same conditions.

The obtained ZnO@LIG nanocomposites show a similar or even more remarkable photocatalytic performance if compared to other systems based on ZnO (alone or in presence of carbon nanomaterials) presented in the literature [30–32], leading to the same or a higher MB discoloration percentage in a comparable or significative lower time of UV irradiation. However, an accurate quantitative comparison of the performance would not be straightforward and conclusive, because of the variability in the experimental set up among different works. Notwithstanding this, it is possible to state that the ZnO@LIG nanocomposites present the advantage of being solid supported if compared to other ZnO systems reported in the literature, thus avoiding the necessity of a separation step for the photocatalyst after the process, without paying a toll to the overall efficiency.

4. Conclusions

In conclusion, we fabricated ZnO@LIG nanocomposites by means of thermal ALD of ZnO on a less porous LIG substrate (LIG-P) and a more porous one (LIG-V). We proved that this technique is especially suitable for achieving an easy and effective deposition of such a semiconductor, coating all the pores of the LIG substrate over the entire cross-section. The adsorption capacity and the photocatalytic activity of the resulting material after a variable number of ALD cycles (100, 200, 400) were evaluated, demonstrating its promising photocatalytic activity towards the photodegradation of organic pollutants in water. In particular, ZnO@LIG-P and ZnO@LIG-V obtained after 400 deposition cycles show

the highest photocatalytic activity under UV irradiation leading to a maximum discoloration percentage of MB at 120 min of nearly 70 %, notwithstanding the high WCA measured for these samples. XRD confirmed the presence of ZnO in both types of nanocomposites; ZnO is proved to grow stoichiometrically even at low number of ALD cycles by XPS measurements, that show a O/Zn ratio of around 1.00. SEM images of FIB cross sections demonstrated that the deposition of ZnO occurs even down to the very bottom of the LIG pores.

Further characterization will be needed to investigate deeply how the porosity and the surface area of the LIG samples have an impact on the ZnO deposition via ALD and, in turn, on the photocatalytic performances of the resulting nanocomposites. Furthermore, the role played by LIG in the photocatalytic mechanism is worth of additional extensive investigation and will be the focus of future work.

CRediT authorship contribution statement

Regina Del Sole: Writing – review & editing, Writing – original draft, Visualization, Investigation, Formal analysis, Data curation, Conceptualization. **Alexander Dallinger:** Writing – review & editing, Writing – original draft, Visualization, Validation, Methodology, Investigation, Formal analysis, Data curation. **Birgit Kunert:** Investigation. **Sreenadh Thaikkattu Sankaran:** Methodology. **Francesco Greco:** Writing – review & editing, Supervision. **Paola Parlanti:** Writing – review & editing, Investigation. **Mauro Gemmi:** Investigation. **Antonella Milella:** Writing – review & editing, Supervision, Project administration, Funding acquisition, Formal analysis, Conceptualization. **Francesco Fracassi:** Writing – review & editing, Supervision. **Anna Maria Coclite:** Writing – review & editing, Supervision, Investigation, Formal analysis, Data curation.

Declaration of competing interest

The authors declare that they have no known competing financial interests or personal relationships that could have appeared to influence the work reported in this paper.

Acknowledgements

Appendix A. Supplementary data

Supplementary data to this article can be found online at https://doi.org/10.1016/j.apsusc.2024.161875.

Data availability

Data will be made available on request.

References

[1] K.U.N.A.L. Mondal, A. Sharma, Photocatalytic oxidation of pollutant dyes in wastewater by TiO_2 and ZnO nano-materials–a mini-review, Nanosci. Technol. Mankind (2014) 36–72.

[2] C. Boon Ong, L. Yong Ng, A.W. Mohammad, A review of ZnO nanoparticles as solar photocatalysts: Synthesis, mechanisms and applications, Renew. Sustain. Energy Rev. 81 (1m) (2018) 536–551, https://doi.org/10.1016/j.rser.2017.08.020.

[3] A.M. Kasumov, K.A. Korotkov, V.M. Karavaeva, M.M. Zahornyi, A.I. Dmitriev, A. I. Ievtushenko, Photocatalysis with the Use of ZnO Nanostructures as a Method for the Purification of Aquatic Environments from Dyes, J. Water Chem. Technol. 43 (2021) 281–288, https://doi.org/10.3103/S1063455X21040044.

[4] S.B. Babar, N.L. Gavade, D.P. Bhopate, A.N. Kadam, S.B. Kokane, S.D. Sartale, A. Gophane, K.M. Garadkar, V.M. Bhuse, An efficient fabrication of ZnO–carbon nanocomposites with enhanced photocatalytic activity and superior photostability, J. Mater. Sci. Mater. Electron. 30 (2019) 1133–1147, https://doi.org/10.1007/s10854-018-0382-5.

[5] V. Noi Nguyen, D. Trinh Tran, M. Tuong Nguyen, T.T. Thuy Le, M. Ngoc Ha, M. Viet Nguyen, T. Dong Pham, Enhanced photocatalytic degradation of methyl orange using ZnO/graphene oxide nanocomposites, Res. Chem. Intermed. 44 (2018) 3081–3095, https://doi.org/10.1007/s11164-018-3294-3.

[6] E.V. Rut`kov, E.Y. Afanas'eva, N.R. Gall, Graphene and graphite work function depending on layer number on Re, Diam. Relat. Mater. 101 (2020) 107576, https://doi.org/10.1016/j.diamond.2019.107576.

[7] B. Xue, Y. Zou, High photocatalytic activity of ZnO–graphene composite, J. Colloid Interface Sci. 529 (2018) 306–313, https://doi.org/10.1016/j.jcis.2018.04.040.

[8] J. Lin, Z. Peng, Y. Liu, F. Ruiz-Zepeda, R. Ye, E.L.G. Samuel, M.Y. Yacaman, B.I. Yakobson, J.M. Tour, Laser-induced porous graphene films from commercial polymers, Nat. Commun. 5 (2014) 5714, https://doi.org/10.1038/ncomms6714.

[9] F.M. Vivaldi, A. Dallinger, A. Bonini, N. Poma, L. Sembranti, D. Biagini, P. Salvo, F. Greco, F. Di Francesco, Three-Dimensional (3D) Laser-Induced Graphene: Structure, Properties, and Application to Chemical Sensing, ACS Appl. Mater. Interfaces 13 (26) (2021) 30245–30260, https://doi.org/10.1021/acsami.1c05614.

[10] Z. Zhang, H. Zhu, W. Zhang, Z. Zhang, J. Lu, K. Xu, Y. Liu, V. Saetang, A review of laser-induced graphene: From experimental and theoretical fabrication processes to emerging applications, Carbon 214 (2023) 118356, https://doi.org/10.1016/j.carbon.2023.118356.

[11] A. Dallinger, K. Keller, H. Fitzek, F. Greco, Stretchable and Skin-Conformable Conductors Based on Polyurethane/Laser-Induced Graphene, ACS Appl. Mater. Interfaces 12 (17) (2020) 19855–19865, https://doi.org/10.1021/acsami.0c03148.

[12] A. Dallinger, F. Steinwender, M. Gritzner, F. Greco, Different Roles of Surface Chemistry and Roughness of Laser-Induced Graphene: Implications for Tunable Wettability, ACS Appl. Nano Mater. 6 (18) (2023) 16201–16211, https://doi.org/10.1021/acsanm.3c02066.

[13] L.X. Duy, Z. Peng, Y. Li, J. Zhang, Y. Ji, J.M. Tour, Laser-induced graphene fibers, Carbon 126 (2018) 472–479, https://doi.org/10.1016/j.carbon.2017.10.036.

[14] M. Abdulhafez, G.N. Tomaraei, M. Bedewy, Fluence-Dependent Morphological Transitions in Laser-Induced Graphene Electrodes on Polyimide Substrates for Flexible Devices, ACS Appl. Nano Mater. 4 (3) (2021) 2973–2985, https://doi.org/10.1021/acsanm.1c00101.

[15] A.C. Bressi, A. Dallinger, Y. Steksova, F. Greco, Bioderived Laser-Induced Graphene for Sensors and Supercapacitors, ACS Appl. Mater. Interfaces 15 (30) (2023) 35788–35814, https://doi.org/10.1021/acsami.3c07687.

[16] T. Wang, B. Tian, B. Han, D. Ma, M. Sun, A. Hanif, D. Xia, J. Shang, Recent advances on porous materials for synergetic adsorption and photocatalysis, Energy & Environmental Materials 5 (3) (2022) 711–730, https://doi.org/10.1002/eem2.12229.

[17] C.M. Tittle, D. Yilman, M.A. Pope, C.J. Backhouse, Robust superhydrophobic laser-induced graphene for desalination applications, Advanced Materials Technologies 3 (2) (2018) 1700207, https://doi.org/10.1002/admt.201700207.

[18] W. Jiang, Y. Zhu, G. Zhu, Z. Zhang, X. Chen, W. Yao, Three-dimensional photocatalysts with a network structure, J. Mater. Chem. A 5 (2017) 5661–5679, https://doi.org/10.1039/C7TA00398F.

[19] B.A. Tesfahunegn, M.N. Kleinberg, C.D. Powell, C.J. Arnusch, A Laser-Induced Graphene-Titanium(IV) Oxide Composite for Adsorption Enhanced Photodegradation of Methyl Orange, Nanomaterials 13 (5) (2023) 947, https://doi.org/10.3390/nano13050947.

[20] J. Rodrigues, J. Zanoni, G. Gaspar, A.J.S. Fernandes, A.F. Carvalho, N.F. Santos, T. Monteiro, F.M. Costa, ZnO decorated laser-induced graphene produced by direct laser scribing, Nanoscale Adv. 1 (2019) 3262, https://doi.org/10.1039/c8na00391b.

[21] N.F. Santos, J. Rodrigues, S.O. Pereira, A.J.S. Fernandes, T. Monteiro, F.M. Costa, Electrochemical and photoluminescence response of laser-induced graphene/electrodeposited ZnO composites, Scientific Reports 11 (2021) 17154, https://doi.org/10.1038/s41598-021-96305-8.

[22] P.O. Oviroh, R. Akbarzadeh, D. Pan, R.A.M. Coetzee, T. Jen, New development of atomic layer deposition: processes, methods and applications, Engineering and Structural Materials 20 (1) (2019) 465–496, https://doi.org/10.1080/14686996.2019.1599694.

[23] A. Perrotta, R. Berger, F. Muralter, A.M. Coclite, Mesoporous ZnO thin films obtained from molecular layer deposited "zincones, Dalton Trans. 48 (2019) 14178, https://doi.org/10.1039/c9dt02824b.

[24] C. Lo Porto, M. Dell'Edera, I. De Pasquale, A. Milella, F. Fracassi, M.L. Curri, R. Comparelli, F. Palumbo, Photocatalytic Investigation of Aerosol-Assisted Atmospheric Pressure Plasma Deposited Hybrid TiO2 Containing Nanocomposite Coatings, Nanomaterials 12 (21) (2022) 3758, https://doi.org/10.3390/nano12213758.

[25] H. Ennaceri, L. Wang, D. Erfurt, W. Riedel, G. Mangalgiri, A. Khaldoun, A. El Kenz, A. Benyoussef, A. Ennaoui, Water-resistant surfaces using zinc oxide structured nanorod arrays with switchable wetting property, Surface and Coatings Technology 299 (2016) 169–176, https://doi.org/10.1016/j.surfcoat.2016.04.056.

[26] P. Scherrer, Bestimmung der Grosse und inneren Struktur von Kolloidteilchen mittels Rontgenstrahlen, Nach Ges Wiss Gottingen 2 (1918) 8–100.

[27] S. Gates-Rector, T. Blanton, The Powder Diffraction File: A Quality Materials Characterization Database, Powder Diffr. 34 (4) (2019) 352–360, https://doi.org/10.1017/S0885715619000812.

[28] A. Di Mauro, M.E. Fragalà, V. Privitera, G. Impellizzeri, ZnO for application in photocatalysis: From thin films to nanostructures, Mater. Sci. Semicond. Process. 69 (2017) 44–51, https://doi.org/10.1016/j.mssp.2017.03.029.

[29] J. Liu, L. Ye, S. Wooh, M. Kappl, W. Steffen, H.-J. Butt, Optimizing Hydrophobicity and Photocatalytic Activity of PDMS-Coated Titanium Dioxide, ACS Appl. Mater. Interfaces 11 (30) (2019) 27422–27425, https://doi.org/10.1021/acsami.9b07490.

[30] G. Zhu, H. Wang, G. Yang, L. Chen, P. Guo, L. Zhang, A facile synthesis of ZnO/CNT hierarchical microsphere composites with enhanced photocatalytic degradation of methylene blue, RSC Adv. 5 (89) (2015) 72476–72481, https://doi.org/10.1039/C5RA11873E.

[31] P. Rong, P. Jiang, O. Wang, M. Gu, X. Jiang, O. Yu, Photocatalytic degradation of methylene blue (MB) with Cu1–ZnO single atom catalysts on graphene-coated flexible substrates, J. Mater. Chem. A 10 (2022) 6231–6241, https://doi.org/10.1039/D1TA09954J.

[32] N.T. Nguyen, V.A. Nguyen, Synthesis, Characterization, and Photocatalytic Activity of ZnO Nanomaterials Prepared by a Green, Nonchemical Route, J. Nanomater. 1 (2020) 2020, https://doi.org/10.1155/2020/1768371.